Research Paper

Study of the ^{13}CO/C^{18}O abundance ratio towards the filamentary infrared dark cloud IRDC 34.43 + 0.24

M. B. Areal[1] , S. Paron[1,2], M. E. Ortega[1] and L. Duvidovich[1]

[1]CONICET-Universidad de Buenos Aires, Instituto de Astronomía y Física del Espacio CC 67, Suc. 28, 1428 Buenos Aires, Argentina and [2]Universidad de Buenos Aires, Facultad de Arquitectura, Diseño y Urbanismo. Buenos Aires, Argentina

Abstract

Nowadays, there are several observational studies about the ^{13}CO/C^{18}O abundance ratio ($X^{13/18}$) towards nearby molecular clouds. These works give observational support to the C^{18}O selective photodissociation due to the interaction between the far ultraviolet (FUV) radiation and the molecular gas. It is necessary to increase the sample of molecular clouds located at different distances and affected in different ways by nearby or embedded H II regions and OB associations to study the selective photodissociation. Using ^{12}CO, ^{13}CO, and C^{18}O J = 1–0 data obtained from the FOREST unbiased Galactic plane imaging survey performed with the Nobeyama 45-m telescope, we analyse the filamentary infrared dark cloud IRDC 34.43 + 0.24 located at the distance of about 3.9 kpc. This infrared dark cloud (IRDC) is related to several H II regions and young stellar objects. Assuming local thermodynamic equilibrium, we obtain: $0.8 \times 10^{16} < $ N(^{13}CO) $ < 4 \times 10^{17}$ cm^{-2} (average value = 4.2×10^{16} cm^{-2}), $0.6 \times 10^{15} < $ N(C^{18}O) $< 4.4 \times 10^{16}$ cm^{-2} (average value = 5.0×10^{15} cm^{-2}), and $3 < X^{13/18} < 30$ (average = 8) across the whole IRDC. Larger values of $X^{13/18}$ were found towards portions of the cloud related to the H II regions associated with the N61 and N62 bubbles and with the photodissociation regions, precisely the regions in which FUV photons are strongly interacting with the molecular gas. Our result represents an observational support to the C^{18}O selectively photodissociation phenomenon occurring in a quite distant filamentary IRDC. Additionally, based on IR data from the Hi-GAL survey, the FUV radiation field was estimated in Habing units, and the dust temperature (T$_{dust}$) and H$_2$ column density (N(H$_2$)) distribution were studied. Using the average of N(H$_2$), values in close agreement with the 'canonical' abundance ratios [H$_2$]/[^{13}CO] and [H$_2$]/[C^{18}O] were derived. However, the obtained ranges in the abundance ratios show that if an accurate analysis of the molecular gas is required, the use of the 'canonical' values may introduce some bias. Thus, it is important to consider how the gas is irradiated by the FUV photons across the molecular cloud. The analysis of $X^{13/18}$ is a good tool to perform that. Effects of beam dilution and clumpiness were studied.

Keywords: Galaxy: abundances—ISM: abundances—*(ISM:)* H II regions—ISM: molecules

(Received 29 June 2019; revised 1 November 2019; accepted 06 November 2019)

1. Introduction

The study of molecular abundances towards molecular clouds located at different environments in the interstellar medium (ISM) is very useful for our knowledge of the chemical evolution of the galaxy. Taking into account that the physical processes that take place in the molecular gas during the born and the evolution of massive stars have a deep influence in the chemistry, the study of molecular abundances towards massive star-forming regions is very important.

Given that the CO is the second most abundant molecule in the ISM, its observation in millimeter wavelengths has been crucial to probe such scenarios (e.g. Goldsmith et al. 2008; Ungerechts & Thaddeus 1987; Solomon et al. 1987). It is known that the far ultraviolet (FUV) radiation selectively dissociates CO isotopes more effectively than CO (e.g. Liszt 2007; Glassgold et al. 1985); thus, the analysis of the ^{13}CO and C^{18}O emission is important for the study

of the influence that the FUV photons have in the molecular gas. As shown by theoretical studies (see for instance, Warin et al. 1996 and van Dishoeck & Black 1988), the selective photodissociation may result from self-shielding effects, which can depend not only on the type of isotope but also on the rotational quantum number J of the molecule. Zielinsky et al. (2000) point out that the clumpiness of the cloud is also important in the analysis of the ^{13}CO/C^{18}O abundance ratio. Due to the self-shielding, the dissociation rate increases with decreasing column density. This effect is more evident for the C^{18}O than for the ^{13}CO as the clump size becomes smaller, which implies that in small clumps the C^{18}O is almost completely dissociated and hence the ^{13}CO/C^{18}O abundance ratio becomes high.

It was found that the C^{18}O is selectively photodissociated with respect to ^{13}CO in many relatively nearby molecular clouds that are exposed in different ways to the radiation field (Yamagishi et al. 2019; Kong et al. 2015; Minchin et al. 1995). Moreover, this effect was analysed in clouds that the selective photodissociation is due to UV radiation from embedded OB stars (e.g. Shimajiri et al. 2014) and clouds that are only affected by the FUV from the interstellar radiation field (e.g. Lin et al. 2016). Therefore, the behaviour of the ^{13}CO/C^{18}O abundance ratio (hereafter $X^{13/18}$)

across molecular clouds could be used as a tool to indirectly evaluate the degree of photodissociation in the cloud (Paron et al. 2018).

Nowadays, there are large molecular line surveys which allow us to estimate molecular abundances ratios towards different environments in the ISM, avoiding the use of indirect estimations from known elemental abundances. For example, the $X^{13/18}$ ratio usually is obtained from the double ratio between the $^{12}C/^{13}C$ and $^{16}O/^{18}O$ (Wilson & Rood 1994). Thus, increasing the sample of molecular clouds in which the $X^{13/18}$ ratio is studied in detail from the direct measurements of the molecular emission is necessary.

It is known that filamentary structures are fundamental building blocks of molecular clouds in the ISM (André et al. 2014; Arzoumanian et al. 2011). They contain enough mass to give birth to high-mass stars and star clusters (e.g. Contreras et al. 2016). These filamentary structures are usually observed as infrared dark clouds (IRDCs), which indeed are sites where massive stars and star clusters born (Rathborne et al. 2006). Therefore, filamentary IRDCs, usually affected by the radiation of nearby and/or embedded H II regions, are interesting sources to study the behaviour of the $X^{13/18}$ abundance ratio.

2. Presentation of IRDC 34.43 + 0.24

We selected the filamentary IRDC 34.43 + 0.24 (Xu et al. 2016; Shepherd et al. 2007) to perform an abundance ratio study. This filament is located at a distance of about 3.9 kpc (Foster et al. 2014), and the distribution and kinematic of the molecular gas was studied by Xu et al. (2016) using the ^{13}CO and $C^{18}O$ J = 1–0 line with an angular resolution of 53 arcsec. As shown by these authors and Shepherd et al. (2007), embedded in this IRDC there are several H II regions and young stellar objects. In particular, the star-forming complex G34.26 + 0.15 (hereafter G34 complex) is associated with this filament, which is composed by several H II regions at different evolutionary stages (Avalos et al. 2009). As the authors point out, a cometary ultracompact (UC) H II region (G34.26 + 0.15C) is the responsible for the most intense emission at radio wavelengths. This UC H II region contains a cluster of OB stars with an O6.5 spectral type the most luminous (Wood & Churchwell 1989). The region also contains a hot core related to H_2O and OH masers (see Imai et al. 2011 and Garay et al. 1985, respectively), which indicate the existence of outflowing activity. Bordering the most compact region of the complex, there are also two large H II regions that are catalogued as infrared dust bubbles (N61 and N62; Churchwell et al. 2006, H II regions G34.172 + 0.175 and G34.325 + 0.211, respectively). Additionally, the UC H II region G34.4 + 0.23, which presents massive molecular outflows, lies towards the north-east of the IRDC (Shepherd et al. 2007).

Figure 1 exhibits the IRDC 34.43 + 0.24 and G34 complex in a three-colour image, in which the borders of the photodissociation regions (PDRs) (displayed in the *Spitzer*-IRAC 8-μm emission in red from the GLIMPSE/Spitzer survey[a]), the distribution of the ionised gas (shown with the 20-cm emission in blue from the New GPS 20-cm survey extracted from the MAGPIS[b]), and the cold dust concentrations (displayed with the continuum emission at 1.1 mm in green obtained from the Bolocam Galactic Plane Survey; Aguirre et al. 2011) are observed. The molecular gas distribution is shown in contours, which represent the $C^{18}O$ J = 1–0 line
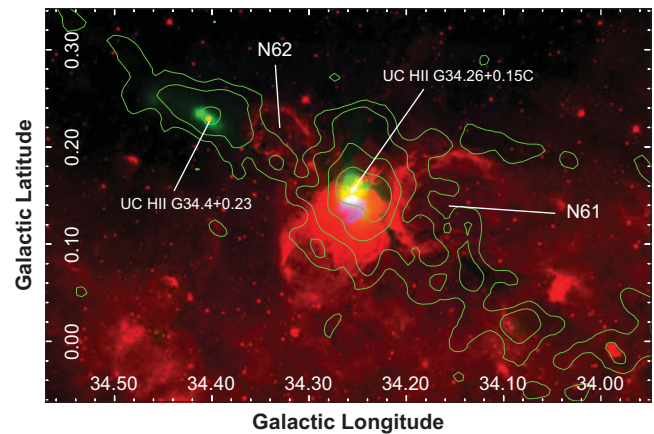
Figure 1. Three-colour image towards G34 complex displaying the *Spitzer*-IRAC 8-μm emission in red, the radio continuum emission at 20 cm as extracted from the MAGPIS in blue, and the continuum emission at 1.1 mm obtained from the Bolocam Survey in green. The green contours are the $C^{18}O$ J = 1–0 emission as presented in Figure 3 (bottom panel).

integrated between 47 and 70 km s^{-1}, which is the velocity range in which this IRDC extends (see Section 3). As shown in Figure 1, the UC H II region G34.26 + 0.15C (G34.26 UC H II in Shepherd et al. 2007) seems to be embedded in a cold dust clump traced by the continuum emission at 1.1 mm. Extended radio continuum emission appears southwards UC H II region G34.26 + 0.15C, which may be related to the IR-bright nebula extending below the UC H II region as described by Shepherd et al. (2007).

3. Data and the estimation of $X^{13/18}$

3.1. Data

The ^{12}CO, ^{13}CO, and $C^{18}O$ J = 1–0 data were obtained from the FOREST unbiased Galactic plane imaging survey performed with the Nobeyama 45-m telescope (FUGIN project; Umemoto et al. 2017)[c]. The angular resolutions are: 20 arcsec for the ^{12}CO data, and 21 arcsec for the ^{13}CO and $C^{18}O$ data. The spectral resolution is 1.3 km s^{-1} for all isotopes.

Graphical Astronomy and Image Analysis Tool (GAIA)[d] and tools from the Starlink software package (Currie et al. 2014) were used to analyse the data. Codes in *python* were developed to obtain the maps of the analysed parameters.

Additionally, we use IR data from the Hi-GAL survey (Molinari et al. 2010), retrieved from the Herschel Science Archive[e]. In particular, maps of Herschel-PACS at 70 and 160 μm (angular resolutions of about 6 and 12 arcsec, respectively), and maps of dust temperature and H_2 column density derived from a SED fit between 70 and 500 μm (Marsh et al. 2017) were used (angular resolution of 36 arcsec).

3.2. $X^{13/18}$ estimation

We carefully inspect the data cubes along the whole velocity range and find that the systemic velocity of the ^{13}CO and $C^{18}O$ is quite
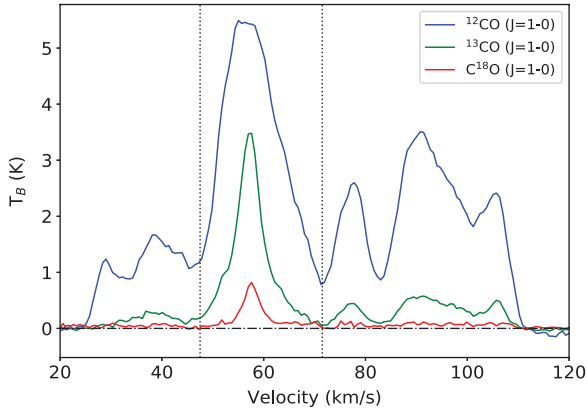
Figure 2. Average ^{12}CO, ^{13}CO, and C^{18}O J = 1–0 spectra towards IRDC 34.43 + 0.24. The vertical dashed lines show the velocity range in which the IRDC extends.

homogeneous across the IRDC. The molecular emission extends from about 47 to 70 km s^{-1}. Figure 2 displays average ^{12}CO, ^{13}CO, and C^{18}O spectra towards the analysed region.

In order to obtain maps of $X^{13/18}$ ($X^{13/18}$ = N(^{13}CO)/N(C^{18}O)), we need to calculate the ^{13}CO and C^{18}O column densities pixel-by-pixel. To do that, we assume local thermodynamic equilibrium (LTE) and a beam filling factor of 1, and we follow the standard procedures (e.g. Mangum & Shirley 2015). The optical depths ($\tau_{^{13}CO}$ and $\tau_{C^{18}O}$) and column densities (N(^{13}CO) and N(C^{18}O)) were derived from the following equations:

$$\tau_{^{13}CO} = -ln \left(1 - \frac{T_{mb}(^{13}CO)}{5.29 \left[\frac{1}{e^{5.29/T_{ex}}-1} - 0.164 \right]} \right) \quad (1)$$

$$N(^{13}CO) = 2.42 \times 10^{14} \frac{T_{ex} + 0.88}{1 - e^{\frac{-5.29}{T_{ex}}}} \int \tau_{^{13}CO} dv \quad (2)$$

with

$$\int \tau_{^{13}CO} dv = \frac{1}{J(T_{ex}) - 0.868} \frac{\tau_{^{13}CO}}{1 - e^{-\tau_{^{13}CO}}} \int T_{mb}(^{13}CO) dv \quad (3)$$

$$\tau_{C^{18}O} = -ln \left(1 - \frac{T_{mb}(C^{18}O)}{5.27 \left[\frac{1}{e^{5.27/T_{ex}}-1} - 0.166 \right]} \right) \quad (4)$$

$$N(C^{18}O) = 2.42 \times 10^{14} \frac{T_{ex} + 0.88}{1 - e^{\frac{-5.27}{T_{ex}}}} \int \tau_{C^{18}O} dv \quad (5)$$

with

$$\int \tau_{C^{18}O} dv = \frac{1}{J(T_{ex}) - 0.872} \frac{\tau_{C^{18}O}}{1 - e^{-\tau_{C^{18}O}}} \int T_{mb}(C^{18}O) dv \quad (6)$$

in which correction for high optical depths was applied (Frerking et al. 1982). This correction is indeed required in the case of ^{13}CO but not for C^{18}O because it is mostly optically thin.

The $J(T_{ex})$ parameter is $\frac{5.29}{exp(\frac{5.29}{T_{ex}})-1}$ and $\frac{5.27}{exp(\frac{5.27}{T_{ex}})-1}$ for equations (3) and (6), respectively. T_{mb} and T_{ex} are the main brightness temperature and the excitation temperature, respectively. Assuming that the ^{12}CO J = 1–0 emission is optically thick, it is possible to derive T_{ex} from:

$$T_{ex} = \frac{5.53}{\ln[1 + 5.53/(^{12}T_{peak} + 0.818)]} \quad (7)$$

where $^{12}T_{peak}$ is the ^{12}CO peak temperature. Thus from maps of $^{12}T_{peak}$, maps of excitation temperatures (T_{ex}) are obtained.
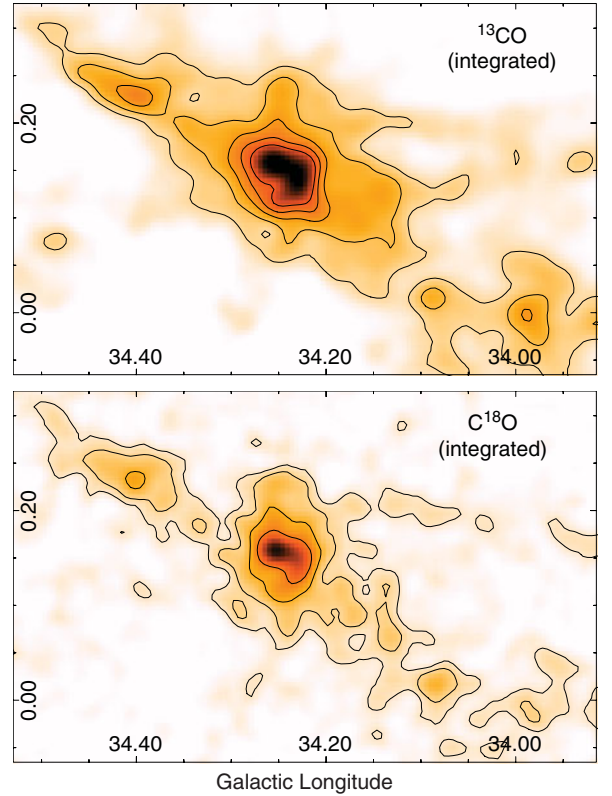
Figure 3. Top and bottom panels: maps showing the ^{13}CO and C^{18}O J = 1–0 line integrated between 47 and 70 km s^{-1}, respectively. The contours levels are 22, 30, 40, 50, and 60 K km s^{-1}, and 4, 6, 10, and 16 K km s^{-1} for the ^{13}CO and C^{18}O, respectively. The angular resolution is 21 arcsec. The sigma levels of these integrated maps are $\sigma_{13} = 4.5$ and $\sigma_{18} = 1.0$ K km s^{-1}.

Before obtaining the column densities maps, we generate ^{13}CO and C^{18}O optical depths (τ^{13} and τ^{18}) maps and check the values.

In some pixels, we notice that τ^{13} becomes undefined due to a negative argument in the logarithm of Equation 1. It is likely that this issue is a consequence of high saturation in the line emission. We investigate the spectra corresponding to such pixels and we find that the ^{12}CO profiles indeed present signs of saturation and self-absorption which may affect the estimate of T_{ex}. Also some ^{13}CO spectra in such pixels, and in others, mainly at the vicinity of the UC G34.26+0.15C, present kinematic signatures of infall (as found by Xu et al. 2016) that prevent us to obtain reliable values of column densities.

4. Results

4.1. Molecular gas

Figure 3 displays the molecular gas distribution associated with the IRDC 34.43 + 0.24 in the ^{13}CO and C^{18}O J=1–0 line integrated between 47 and 70 km s^{-1}, with an angular resolution of 21 arcsec. The lowest contour of the integrated C^{18}O is 4σ. We consider it as a threshold to study the abundance ratio and others physical parameters derived in this work, that is, all the analyses are done for the region contained by this C^{18}O contour.

Figure 4 shows a map of the excitation temperature obtained from the ^{12}CO J = 1–0 emission following equation (7), and Figure 5 displays the maps of the obtained ^{13}CO and C^{18}O optical depths. Figure 6 presents the obtained maps of the ^{13}CO and C^{18}O
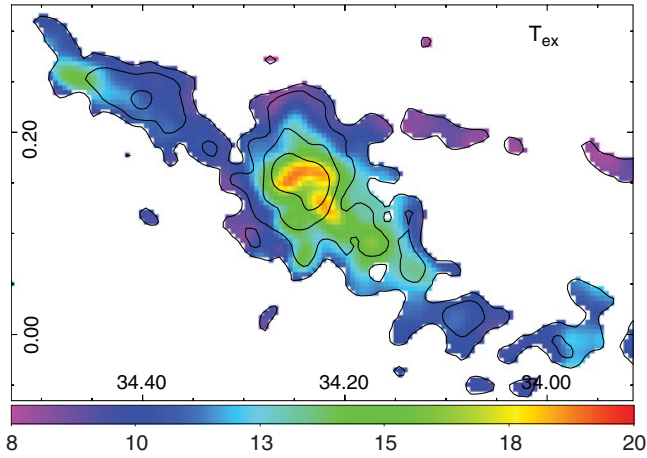
Figure 4. Excitation temperature map derived from the ^{12}CO J = 1–0 emission in the region of the C^{18}O emission. For reference, the C^{18}O contours presented in Figure 3 (bottom panel) are included.
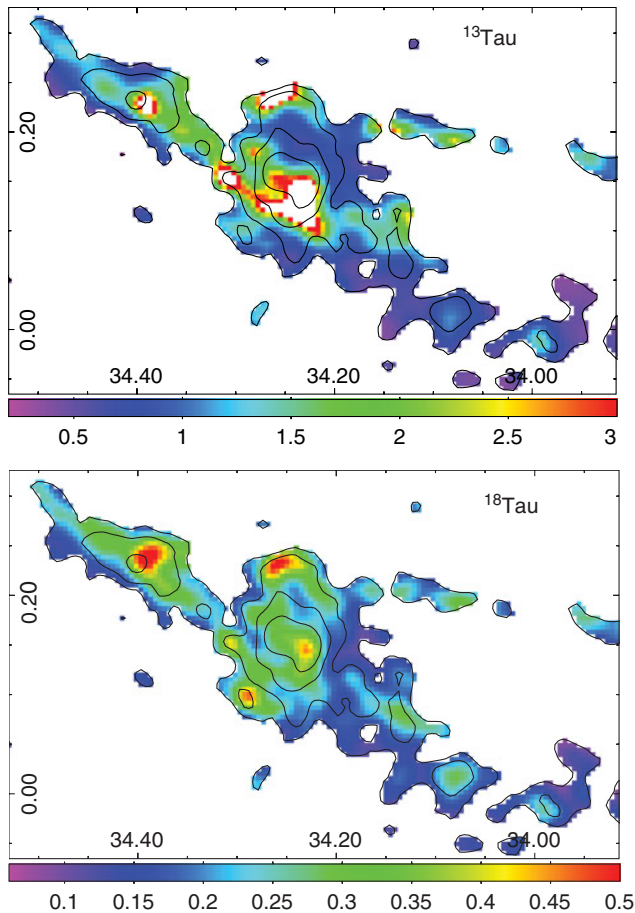
Figure 5. Maps showing the ^{13}CO and C^{18}O optical depths (top and bottom panels, respectively). Contours of the integrated C^{18}O J = 1–0 emission are included for reference.

column densities and the derived abundance ratio $X^{13/18}$. Figure 7 shows the integrated line ratio ($R^{13/18} = \int T^{13} dv / \int T^{18} dv$), and Table 1 presents ranges and averages values of the physical parameters obtained from our analysis.
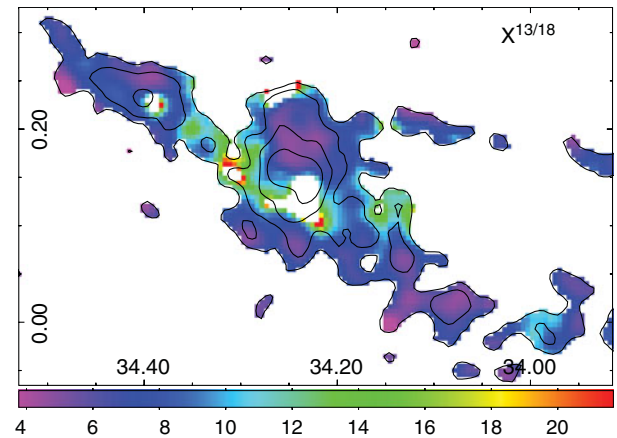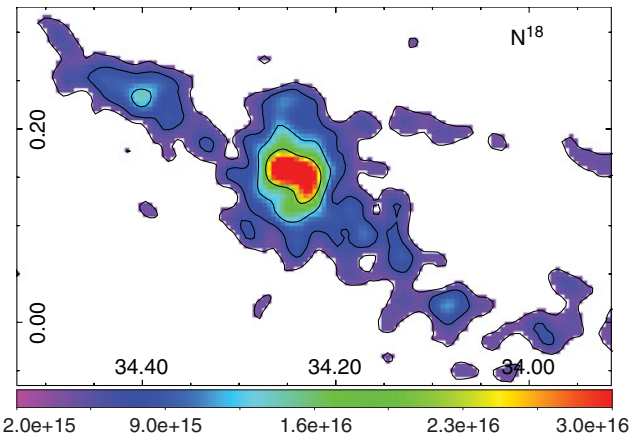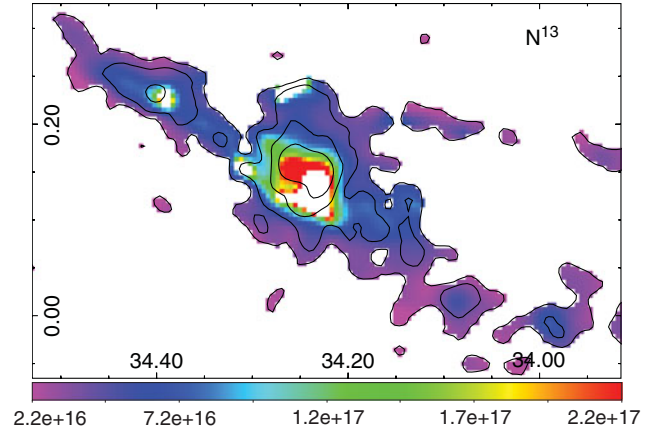

Figure 6. Top and middle panels: maps showing the ^{13}CO and C^{18}O column densities, respectively. The colourbars are in units of cm^{-2}. Bottom panel: the abundance ratio $X^{13/18}$. Contours of the integrated C^{18}O J = 1–0 emission are included for reference.

Figure 8 shows the relation between the abundance ratio $X^{13/18}$ and the integrated line ratio $R^{13/18}$ obtained from different sectors of the molecular cloud defined by the C^{18}O contours: Region A (pixels lying between the contours at 4 and 6 K km s^{-1}), Region B (pixels between contours 6 and 10 K km s^{-1}), Region C (pixels between contours 10 and 16 K km s^{-1}), and Region D (pixels within the contour at 16 K km s^{-1}). The slopes (m) and correlations factors (r) from linear fittings for each case are included in the figure.

Table 1. Ranges of physical parameters.

	T_{ex} [K]	τ^{13}	τ^{18}	$N(^{13}CO)$ [$\times 10^{17}$ cm^{-2}]	$N(C^{18}O)$ [$\times 10^{16}$ cm^{-2}]	$X^{13/18}$	$R^{13/18}$
Ranges	8 – 19	0.2 – 5.7	0.06 – 0.50	0.08 – 4.00	0.06 – 4.40	3 – 30	2.4 – 9.6
Average	11	0.8	0.18	0.42	0.50	8	5.2
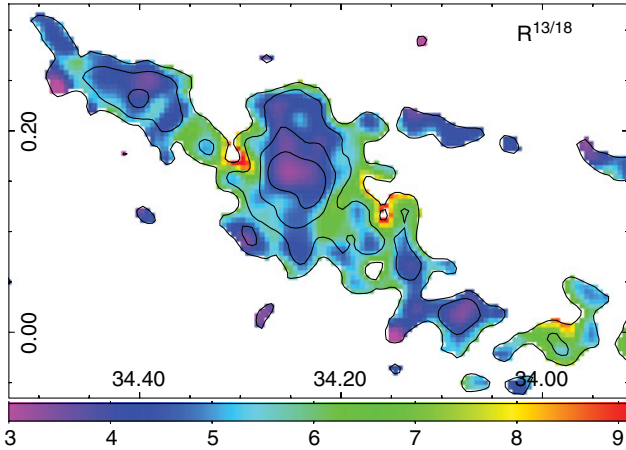
Figure 7. Integrated line ratio ($R^{13/18}$). Contours of the integrated C^{18}O J = 1–0 emission are included for reference.
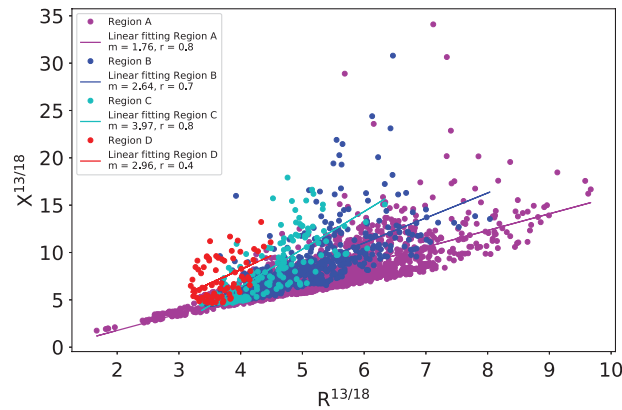
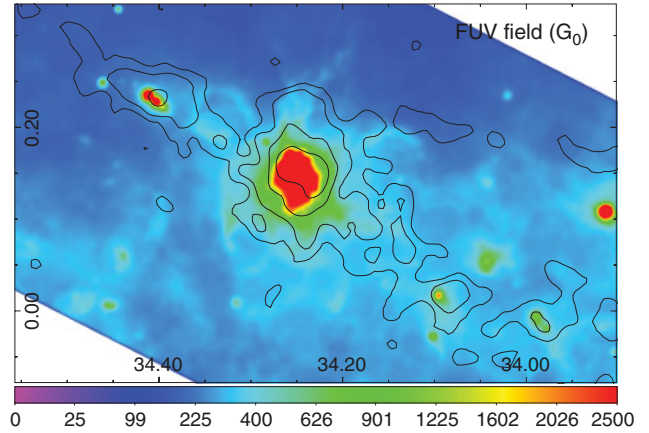**Figure 8.** Abundance ratio ($X^{13/18}$) vs. integrated line ratio ($R^{13/18}$). Region A, B, and C correspond to pixels between the C^{18}O J = 1–0 contours 4 and 6, 6 and 10, and 10 and 16 K km s^{-1}, respectively, and Region D corresponds to pixels within the 16 K km s^{-1} C^{18}O contour. Slopes (m) and correlations factors (r) from linear fittings are included.

Figure 9. Far ultraviolet flux G_0 in units of Habing field. The angular resolution of the image is 21 arcsec. Contours of the integrated C^{18}O J = 1–0 emission are included for reference.

Figure 10. Far ultraviolet flux G_0 in units of Habing field towards the centre of the analysed region. The angular resolution of the image is about 12 arcsec. Contours of the radio continuum emission at 20 cm are presented with levels of 0.02, 0.05, 0.10, 0.15, and 0.20 Jy beam^{-1}.
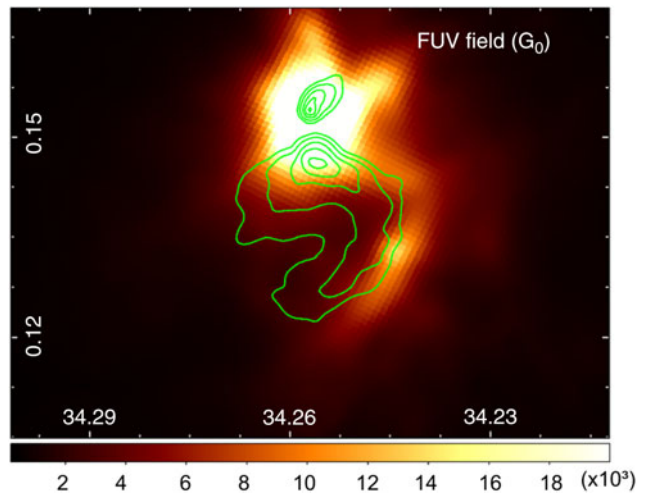
4.2. Determining the FUV radiation field

Given that the clouds seen in far-IR (FIR) are mainly heated by FUV radiation, it is possible to estimate the FUV radiation field from the observed FIR intensity (I_{FIR}) (see Kramer et al. 2008). We compute the FUV radiation field from the FIR intensity in the 60–200 μm range using the Herschel-PACS 70- and 160-μm maps. These maps were convolved to the resolution of the molecular data, and following the procedure explained in Roccatagliata et al. (2013), we generate the FUV radiation map in units of the Habing field from:

$$G_0 = \frac{4\pi I_{FIR}}{1.6 \times 10^{-3} \text{ erg cm}^{-2} \text{ s}^{-1}}, \quad (8)$$

which is presented in Figure 9. Besides, in Figure 10, we present the same FUV radiation field towards the centre of the analysed region where the UC H II region G34.26+0.15C and the radio continuum

shell lie. To do this map with the best angular resolution as possible, the image of PACS 70 μm was convolved to the angular resolution of the PACS 160-μm map (about 12 arcsec), and the same procedure done for the map of Figure 9 was applied. Contours of the radio continuum emission are included to analyse the ionised gas component in relation to the FUV radiation.
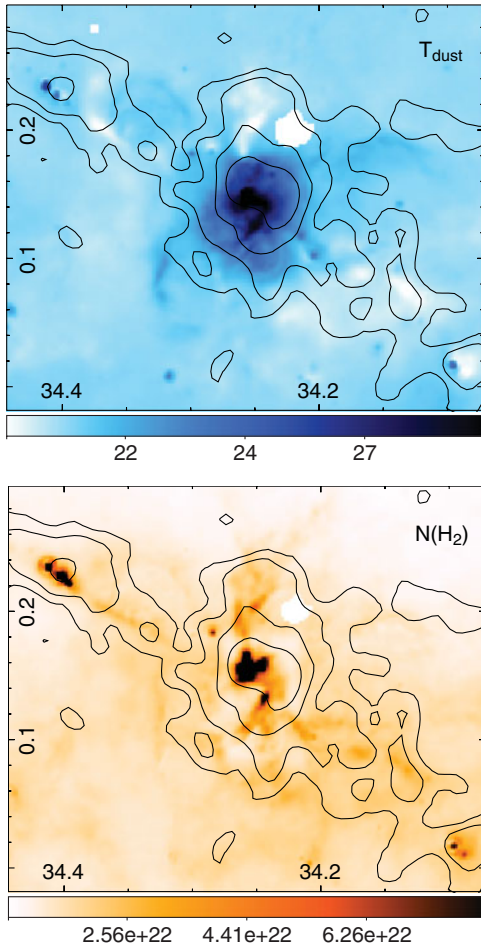
4.3. T_{dust} and $N(H_2)$ towards the centre of the IRDC

To make comparisons between the emissions of the molecular gas and the dust, we obtain maps[f] of the dust temperature and

[f]http://www.astro.cardiff.ac.uk/research/ViaLactea/

Table 2. Parameters derived from the IR data.

	T_{dust} [K]	$N(H_2)$ [$\times 10^{22}$ cm^{-2}]	$N(H_2)/N(^{13}CO)$ [$\times 10^5$]	$N(H_2)/N(C^{18}O)$ [$\times 10^6$]
Ranges	18–33	0.5–3.8	0.6–7.0	0.4–20
Average	20.4	1.5	3.9	3.0

Figure 11. Maps of dust temperature (top) and H$_2$ column density (bottom) obtained from http://www.astro.cardiff.ac.uk/research/ViaLactea/. The colourbars are in units of K and cm^{-2}, respectively. Contours of the integrated C^{18}O J=1–0 are presented for reference.

H$_2$ column density N(H$_2$) (see Figure 11) which were generated from the PPMAP procedure done to the Hi-GAL maps in the wavelength range 70–500 μm (Marsh et al. 2017).

Ranges of dust temperature (T$_{dust}$) and N(H$_2$) with the average values are presented in Table 2. Additionally, after convolving the N(^{13}CO) and N(C^{18}O) maps to the angular resolution of the N(H$_2$) map (about 36 arcsec), we generate maps of N(H$_2$)/N(^{13}CO) and N(H$_2$)/N(C^{18}O) (see Figure 12) whose ranges and average values are also presented in Table 2.

To investigate the dependence of $X^{13/18}$ on the visual extinction towards this IRDC, we obtain an A$_V$ map from the N(H$_2$) following the relation from Bohlin et al. (1978)

$$A_V = \frac{N(H_2)}{9.4 \times 10^{20} \text{cm}^{-2}}. \qquad (9)$$

The map of $X^{13/18}$ was convolved to the angular resolution of the A$_V$ map and in Figure 13 we present plots of $X^{13/18}$ vs. A$_V$.
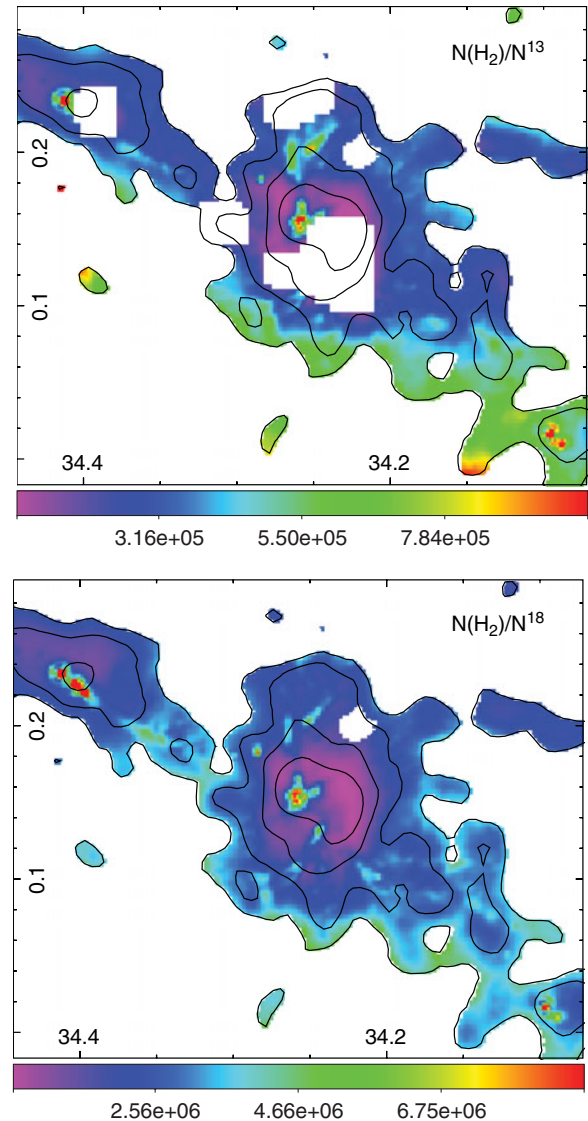
Figure 12. Maps of N(H$_2$)/N(^{13}CO) and N(H$_2$)/N(C^{18}O). The angular resolution of these maps is about 36 arcsec. Contours of the integrated C^{18}O J=1–0 are presented for reference.

5. Discussion

The molecular emission extends along the whole filamentary structure of IRDC 34.43 + 0.24, and as shown in Figure 3, the morphology of the C^{18}O emission is narrower and fits better with the infrared emission from IRDC than the ^{13}CO one. The ranges of N(^{13}CO), N(C^{18}O), and $X^{13/18}$ are quite similar to those found towards the Orion-A giant molecular cloud by Shimajiri et al. (2014). Additionally, our range of values of $X^{13/18}$ also is in agreement with those values found towards LDN 1551, a nearby and isolated star-forming region (Lin et al. 2016). Thus, our results show that $X^{13/18}$ may have a similar behaviour among regions that are located at very different distances from us. The obtained $X^{13/18}$ average value (about 8) across the IRDC is larger than the solar system value of 5.5.

Assuming a distance of 3.9 kpc to IRDC 34.43 + 0.24, a galactocentric distance of about 5.7 kpc is obtained, and following the relation between atomic ratios and the galactocentric distance presented in Wilson & Rood (1994), a $X^{13/18}$ of 7.4 is derived.
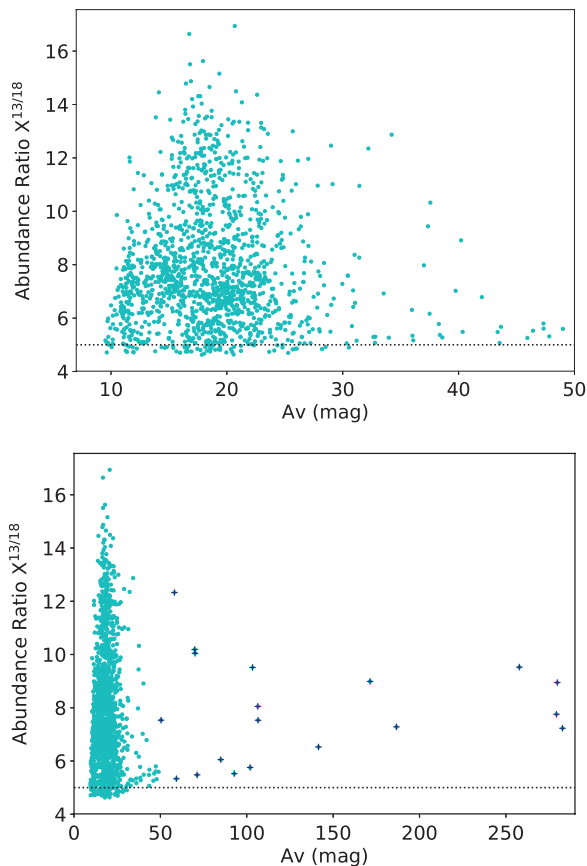
Figure 13. Correlation between $X^{13/18}$ and the visual absorption A_V up to $A_V = 50$ mag (top panel) and along the whole A_V range (bottom panel). In bottom panel, the points corresponding to pixels at the positions of the UC H II regions and their close surroundings are marked with blue crosses.

While this value is in quite agreement with our average value of $X^{13/18}$, it does not reflect the wide range of values found across the molecular cloud. Therefore, it is important to remark that assuming the 'canonical' $X^{13/18}$ from Wilson & Rood (1994) may introduce some bias in the analysis of the molecular gas, mainly in regions that are exposed to FUV radiation.

Figure 6 (bottom panel) shows that highest values in $X^{13/18}$ are found towards regions related to the interiors and/or borders of N61 and N62 bubbles. This can be explained through selective photodissociation of the $C^{18}O$ molecule due to the radiation responsible for the bubbles generation, which may represents an observational support to the $C^{18}O$ selectively photodissociation phenomenon, as found towards other nearby galactic regions (e.g. Yamagishi et al. 2019; Lin et al. 2016; Kong et al. 2015) but in a quite distant filamentary IRDC. In general, an increase in $X^{13/18}$ is observed near the PDRs (see the 8-μm emission in Figure 1), precisely the regions in which FUV photons are interacting with the molecular gas. From the FIR intensity, we estimate the FUV radiation field, which mainly reflects the action of the FUV photons in the dust. An increase in the FUV radiation field is observed towards the G34 complex, where the UC H II region G34.26 + 0.15C lies, and towards the position of UC H II region G34.4 + 0.23 at the north-east of the IRDC (see Figure 9). By comparing the FUV map with the $X^{13/18}$ map, two possible aspects of the influence of the UC H II regions in the abundance ratio can be inferred: in clumps far from the UC H II regions, some $X^{13/18}$ minimums coincide with $C^{18}O$ maximums, while in regions

related to the clumps where the UC H II regions are embedded, this correlation is broken. It is likely that the dust (which reflects the FUV field) may shield the molecular gas, and hence it is not possible to analyse a direct correlation between the $X^{13/18}$ factor and the FUV radiation field derived from the FIR emission.

From a comparison between the radio continuum emission and the FUV radiation field (Figure 10), it is worth noting that the observed radio continuum shell, which represents ionised gas due to Lyman photons, is surrounded by the FUV radiation field, showing the typical stratification of a PDR in H II regions (e.g. Draine 2011).

By comparing the maps of $X^{13/18}$ and $R^{13/18}$, that is, comparing values that were derived from the LTE assumption with values from direct measurements, a quite similar behaviour can be appreciated across the region. The plot $X^{13/18}$ vs. $R^{13/18}$ shows a linear tendency with an increase in the slope as we analyse more dense regions in the cloud (see Figure 8). This behaviour may be explained by a major increase in τ^{13} with respect to τ^{18}. On the other side, Region D shows a low correlation factor, which may be due to that in this region some ^{13}CO spectra present kinematic signatures of infall, and thus, the LTE assumption would no longer be valid in some pixels corresponding to it.

Assuming that the gas and dust are coupled, we can compare the ^{13}CO and $C^{18}O$ column densities obtained from the molecular lines with the $N(H_2)$ derived from the dust emission. The obtained average ratio $N(H_2)/N(^{13}CO)$ of about 4×10^5 is in close agreement with the typical abundance ratio extensively used in the literature ($N(H_2)/N(^{13}CO) = 5 \times 10^5$, e.g. Pineda et al. 2008, and references therein). The average ratio $N(H_2)/N(C^{18}O)$ of 3.0×10^6 obtained in this work is in quite agreement with the typical $[H_2]/[C^{18}O]$ ratio (5.8×10^6, e.g. Frerking et al. 1982).

Additionally, we compare $X^{13/18}$ with the visual absorption A_V derived from $N(H_2)$. The maximum in $X^{13/18}$ occurs between 17 and 22 mag, and the behaviour of this relation is similar as found in previous works (e.g. Kong et al. 2015; Kim et al. 2006; Lada et al. 1994). In our case, an increase in $X^{13/18}$ with respect to A_V can be inferred towards the highest A_V values. We conclude that this plot shows selective photodissociation generated by both, external radiation (probably from the interstellar radiation field (Lin et al. 2016), and/or radiation from surrounding sources such as bubbles N61 and N62) and radiation from deeply embedded sources such as the UC H II regions.

5.1. Beam filling factor effects and clumpiness

It is known that the clouds are highly structured on the subparsec scale implying beam filling factors less than the unity. We investigate the influence of a possible beam dilution effect in the $X^{13/18}$. The beam filling factor can be estimated from (Kim et al. 2006): $\phi = \frac{\theta^2_{source}}{\theta^2_{source} + \theta^2_{beam}}$ where θ^2_{source} and θ^2_{beam} are the source and beam sizes, respectively. The beam size of ^{13}CO and $C^{18}O$ J = 1–0 data is 20 arcsec, which corresponds to 0.37 pc at the distance of 3.9 kpc. From the emission with the best angular resolution used in this work, that is, *Herschel*-PACS 70 μm (angular resolution ∼5 arcsec), we determine that the sizes of clumps in the region are expected to exceed 0.7 pc. Thus, the beam filling factor of the used molecular data is expected to exceed 0.4. Given that the ^{13}CO traces more extended molecular components than the $C^{18}O$, we consider the limit case in which $\phi_{^{13}CO} = 1$ and $\phi_{C^{18}O} = 0.4$. Thus, $X^{13/18}$ could be overestimated up to 60%.

Taking into account that the beam dilution effect would be more important towards the densest/clumpy regions (mainly

traced by the C^{18}O emission) than in regions with diffuse gas, the actual $X^{13/18}$ value should be smaller than the measured one in clumpy regions. This is in agreement with Zielinsky et al. (2000), who point out that as the C^{18}O emitting regions have much smaller extent than the ^{13}CO ones, resulting in a lower area filling factor, and also lower temperatures, larger (i.e. overestimated) $X^{13/18}$ values may be observed. Anyway, if the beam dilution is considered in these regions, the behaviour of $X^{13/18}$ across the whole IRDC would highlight even more the effects of the selective photodissociation.

6. Conclusions

We carried out a large-scale analysis of the abundance ratio $X^{13/18}$ along the filamentary IRDC 34.43 + 0.24 using the ^{12}CO, ^{13}CO, and ^{13}CO J = 1–0 emission with an angular resolution of about 20 arcsec.

In the line of previous works towards relative nearby molecular clouds, we find strong observational evidences supporting the C^{18}O selectively photodissociation due to the FUV photons in a quite distance filamentary IRDC. A range of $X^{13/18}$ between 3 and 30 was found across the molecular cloud related to the IRDC, with an average value of 8, larger than the typical solar value of about 5. From the FIR intensity, we estimate the FUV radiation field, which mainly reflects the action of the FUV photons in the dust. We conclude that it is not possible to analyse a direct correlation between the $X^{13/18}$ and the FUV radiation field derived from the FIR emission because it is likely that in some regions the dust may shield the molecular gas from the FUV photons.

From a comparison between $X^{13/18}$ and the visual absorption A_V, we conclude that selective photodissociation can be generated by both the interstellar radiation field and/or radiation from surrounding H II regions (i.e. external radiation), and radiation from deeply embedded sources in the IRDC.

The average values of $X^{13/18}$, N(H$_2$)/N(^{13}CO), and N(H$_2$)/N(C^{18}O), in which the N(H$_2$) was independently estimated from the dust emission, are in quite agreement with the 'canonical' values used in the literature. However, works like this show that if an accurate analysis of the molecular gas is required, the use of these 'canonical' values may introduce some bias. In those cases, how the gas is irradiated by FUV photons and the implications of beam dilution should be considered, which can affect in different ways the abundance ratios.

References

Aguirre, J. E., et al. 2011, ApJS, 192, 4

André, P., Di Francesco, J., Ward-Thompson, D., Inutsuka, S.-I., Pudritz, R. E., & Pineda, J. E. 2014, Protostars and Planets VI, 27–51

Arzoumanian, D., et al. 2011, A&A, 529, L6

Avalos, M., Lizano, S., Franco-Hernández, R., Rodríguez, L. F., Moran, J. M. 2009, ApJ, 690, 1084

Bohlin, R. C., Savage, B. D., & Drake, J. F. 1978, ApJ, 224, 132

Churchwell, E., Povich, M. S., Allen, D., et al. 2006, ApJ, 649, 759

Contreras, Y., Garay, G., Rathborne, J. M., & Sanhueza, P. 2016, MNRAS, 456, 2041

Currie, M. J., Berry, D. S., Jenness, T., Gibb, A. G., Bell, G. S., & Draper, P. W. 2014, in Astronomical Society of the Pacific Conference Series, ed. N. Manset N. & P. Forshay, Vol. 485, Astronomical Data Analysis Software and Systems XXIII, 391

Draine, B. T. 2011, Physics of the Interstellar and Intergalactic Medium. Princeton University Press, ISBN: 978-0-691-12214-4.

Foster, J. B., et al. 2014, ApJ, 791, 108

Frerking, M. A., Langer, W. D., & Wilson, R. W. 1982, ApJ, 262, 590

Garay, G., Reid, M. J., & Moran, J. M. 1985, ApJ, 289, 681

Glassgold, A. E., Huggins, P. J., & Langer, W. D. 1985, ApJ, 290, 615

Goldsmith, P. F., Heyer, M., Narayanan, G., Snell, R., Li, D., & Brunt, C. 2008, ApJ, 680, 428

Imai, H., Omi, R., Kurayama, T., Nagayama, T., Hirota, T., Miyaji, T., & Omodaka, T. 2011, PASJ, 63, 1293

Kim, S.-J., Kim, H.-D., Lee, Y., Minh, Y. C., Balasubramanyam, R., Burton, M. G., Millar, T. J., & Lee, D.-W., 2006, ApJS, 162, 161

Kong, S., Lada, C. J., Lada, E. A., Román-Zúñiga, C., Bieging, J. H., Lombardi, M., Forbrich, J., & Alves, J. F. 2015, ApJ, 805, 58

Kramer, C., et al. 2008, A&A, 477, 547

Lada, C. J., Lada, E. A., Clemens, D. P., & Bally, J. 1994, ApJ, 429, 694

Lin, S.-J., et al. 2016, ApJ, 826, 193

Liszt, H. S. 2007, A&A, 476, 291

Mangum, J. G., & Shirley, Y. L. 2015, PASP, 127, 266

Marsh, K. A., et al. 2017, MNRAS, 471, 2730

Minchin, N. R., White, G. J., & Ward-Thompson, D. 1995, A&A, 301, 894

Molinari, S., et al. 2010, PASP, 122, 314

Paron, S., Areal, M. B., & Ortega, M. E. 2018, A&A, 617, A14

Pineda, J. E., Caselli, P., & Goodman, A. A. 2008, ApJ, 679, 481

Rathborne, J. M., Jackson, J. M., & Simon, R. 2006, ApJ, 641, 389

Roccatagliata, V., Preibisch, T., Ratzka, T., & Gaczkowski, B. 2013, A&A, 554, A6

Shepherd, D. S., et al. 2007, ApJ, 669, 464

Shimajiri, Y., et al. 2014, A&A, 564, A68

Solomon, P. M., Rivolo, A. R., Barrett, J., & Yahil, A. 1987, ApJ, 319, 730

Umemoto, T., et al. 2017, PASJ, 69, 78

Ungerechts, H., & Thaddeus, P. 1987, ApJS, 63, 645

Warin, S., Benayoun, J. J., & Viala, Y. P. 1996, A&A, 308, 535

Wilson, T. L., & Rood, R. 1994, ARA&A, 32, 191

Wood, D. O. S., & Churchwell, E. 1989, ApJS, 69, 831

Xu, J.-L., Li, D., Zhang, C.-P., Liu, X.-L., Wang, J.-J., Ning, C.-C., & Ju, B.-G. 2016, ApJ, 819, 117

Yamagishi, M., et al. 2019, ApJ, 875, 62

Zielinsky, M., Stutzki, J., & Störzer, H. 2000, A&A, 358, 723

van Dishoeck, E. F., & Black, J. H. 1988, ApJ, 334, 771